

Research Article

Yingjing Liang, Huiyi He, Jun Yin, Yijie Liu, Jianzhang Huang, Zhigang Wu, Yun Zhai, David Hui, and Lewei Yan*

Energy absorption of gradient triply periodic minimal surface structure manufactured by stereolithography

<https://doi.org/10.1515/rams-2023-0185>
received October 11, 2023; accepted February 02, 2024

Abstract: Triply periodic minimal surface (TPMS) metamaterials possess exceptional properties not commonly found in natural materials. TPMS metamaterials are used in lightweight structures and impact energy absorption structures due to their surface geometry and mechanical properties. The quasi-static mechanic properties of resin-based homogeneous and gradient TPMS structures manufactured by stereolithography are investigated in this study. The results of both experimental and numerical simulations reveal that the gradient TPMS structures have superior energy absorption abilities compared to the homogeneous TPMS structures. Furthermore, the benefits of gradient TPMS structures can be further enhanced by changing the gradient variation interval of the relative density and cell thickness of TPMS. If the slope and intercept of the C value function of the TPMS structures remain constant, selecting a design where the gradient direction of the cell aligns with the direction of the load on the material can enhance the energy absorption capability of the TPMS structures.

Keywords: triply periodic minimal surface, additive manufacturing technique, Quasi-static compression, energy absorption, deformation mechanism

1 Introduction

Porous structures have become increasingly popular due to their lightweight properties and exceptional energy absorption abilities [1]. They can be broadly divided into two-dimensional, such as honeycomb structures, and three-dimensional structures [2]. Three-dimensional structures can be further classified into random and ordered distributions. For example, foam structures, bones, and certain plants are primarily randomly distributed 3D structures, while lattices and trusses consist of ordered porous structures.

Triply periodic minimal surface (TPMS) structures belong to ordered porous three-dimensional lattice structures, with surfaces with zero mean curvature, making them mathematically defined with a large surface area [3]. Research has indicated that TPMS metamaterial structures exhibit superior mechanical properties [4] in comparison to traditional porous structures, including less stress concentration [5], high specific energy absorption (SEA), and high specific strength. This makes them ideal for load-bearing and mechanical applications, making them suitable for use in automotive, aerospace [6,7], materials science [8–10], and biological tissue engineering industries [11–14].

Gradient porous structures are ideal for creating lightweight and resistant components that can absorb high levels of energy [15,16]. The function and density of the gradient structures are impacted by the shape, sizes, and wall thicknesses of cells [17], while the composition, porosity, and microstructure of gradient structures dictate their properties. Research by Liu *et al.* [18] has explored the impact of heterostructure and density, focusing on the mechanical properties of a functionally graded porous scaffold made with Ti–6Al–4V alloy, in which density, heterostructure, and cell-size gradient were also considered. Al-Saedi *et al.* [19] have compared the mechanical properties of gradient structures vs those of homogeneous structures under compressive loading and have discovered that functional gradient structures are more suitable for

* Corresponding author: Lewei Yan, School of Civil Engineering, Guangzhou University, Guangzhou 510006, China,
e-mail: ylw21@gzhu.edu.cn

Yingjing Liang, Huiyi He, Jun Yin, Yijie Liu, Jianzhang Huang, Zhigang Wu: School of Civil Engineering, Guangzhou University, Guangzhou 510006, China

Yun Zhai: School of Mechanical Engineering, Dalian Jiaotong University, Dalian, 116028, China

David Hui: Department of Mechanical Engineering, University of New Orleans, New Orleans, LA 70148, United States of America

certain applications. Gradient TPMS structures, in particular, can be designed to achieve complex and multi-directional grading and have been found to have better mechanical properties when compared to homogeneous TPMS structures [20–23]. Ma *et al.* [22] have demonstrated that gradient TPMS structures exhibited a layer-by-layer deformation mechanism. Research scholars have explored that the stress of TPMS exhibited significant post-yield periodic or non-periodic drop and recovery. Failure behavior and deformation mechanism of TPMS sheet lattices exhibited localized shear bands or layer crushing in low relative densities [24]. The design of the cell and relative density significantly impact the energy absorption performance of TPMS metamaterial structures. Yu *et al.* [23] have found that the gradient structure with a Primitive (P) surface exhibited better energy absorption capacity than the homogeneous P structure under quasi-static compressive loading. However, the gradient Gyroid (G) structure showed little difference in energy absorption capacity compared to the homogeneous G structure. Also, the influence of relative density on the energy absorption performance of gradient TPMS structures has not been sufficiently studied. Existing studies do not cover a wide range of relative density settings and focus primarily on lower relative density ranges [23,25,26]. Further systematic analysis is necessary to determine whether the gradient structure has advantages over the homogeneous structure at low relative densities and to examine the factors affecting the energy absorption of gradient TPMS structure and homogeneous structure and their influencing mechanisms. The effect of gradient and multiple gradients on the mechanical properties of structure also needs to be investigated. With the rapid development of additive manufacturing (AM) techniques in recent years, different gradient TPMS structures can be prepared that are adaptable in various fields.

AM is a promising way to manufacture structures with complex geometric configurations. Among the many polymer printing technologies available, stereolithography (SLA) is currently one of the most popular due to its exceptional printing accuracy. SLA employs liquid photosensitive resin polymers as raw material [27]. At the same time, a laser beam or UV light is used to cure liquid polymers layer by layer, building 3D structures on a build platform [28]. SLA technology has various advantages compared to other AM methods, including high printing system stability, fast object forming speed, micron-level precision forming accuracy, and high energy efficiency [29]. As a result, more studies in recent years have utilized SLA for preparing TPMS structures [30–34]. Current research on TPMS has focused on the advantages of lightweight and high energy absorption for practical applications. However, it is also important to

consider accuracy in specimen preparation and raw material utilization during the AM process. The resin polymers ClearV4 and SLA are suitable for creating specimens with small features and a good surface finish. SLA AM technology can achieve high geometrical matching and good surface quality for TPMS structures [35]. Resin TPMS specimens can attain optimal mechanical properties by employing this technique, which enhances the practical application performance and extends the scope of TPMS while ensuring high utilization rates of raw materials.

This study selects the P surface structure to deepen the understanding of the mechanical properties of TPMS structures and the effect of the different gradients. Different TPMS structures are generated based on the implicit function expression of TPMS with different C values. ClearV4 is used as the substrate, and specimens with relative densities of 20, 30, 40, and 50% are fabricated by SLA AM technology. The specimens are characterized and analyzed using a Scanning Electron Microscope (SEM). The mechanical properties of homogeneous P structures and linearly gradient P structures are compared by experiments and verified by finite element analysis (FEA). Furthermore, numerical simulations of different types of gradient structures are carried out by FEA. Additionally, the energy absorption capacity and impact resistance of TPMS structures with different directions, gradients, and multi-gradients are further discussed.

2 Materials and methods

The implicit method uses a single-valued function of three variables, and TPMS is the trajectory of a point for which this function has some constant value. It can be generally approximated as [36]

$$\phi(\mathbf{r}) = \sum_{k=1}^K A_k \cos\left[\frac{2\pi(\mathbf{h}_k \cdot \mathbf{r})}{\lambda_k} + P_k\right], \quad (1)$$

where \mathbf{r} is the position vector in Euclidean space, on the Cartesian coordinate system $\mathbf{r} = (x, y, z)$, and \mathbf{h}_k is the k th lattice vector in the inverse space, A_k , λ_k , and P_k , are the amplitude, period factor, phase function, and constant values, respectively. Based on this, the P surface can be described by a simple trigonometric function as follows:

$$\phi(\mathbf{r}) = \cos(\omega x) + \cos(\omega y) + \cos(\omega z) = C, \quad (2)$$

where $\omega = 2\pi/a$, a is the cell parameter. (x, y, z) are the geometric points in the 3D geometric space. The C value is an important parameter in the composition of TPMS, and the C value affects the shape change and the pore size of

TPMS [37]. When the C value takes a positive value, the pore size of the surface shrinks, while when the C value takes a negative value, the surface expands (as shown in Figure 1), and the range of the C value is $-1 \leq C \leq 1$.

As shown in Figure 1, the cavity part of the primitive surface changes in different forms when the C value is positive or negative. Based on this phenomenon, if we assume that the value of C is always positive and construct two types of primitive surfaces as shown in Figure 2(a), $f(x, y, z) = -C$ and $f(x, y, z) = C$, we can obtain the open dual primitive surfaces in the same cubic space.

The open dual surfaces form the inner and outer boundaries of the P surface structure, and the surfaces form a spatial domain between them with the functional expression [38] as $-C \leq f(x, y, z) \leq C$. The closed primitive surface cell unit is obtained by closing its boundary at the opening formed by the dual surface, and the spatial distance from the inner surface along the direction of the normal to the outer surface is the thickness of the cell unit H . The primitive surface is then topologized from the closed surface into a solid structure (as in Figure 2(b)).

When the absolute C value of the inner and outer surfaces of the TPMS solid cell is constant (e.g., Figure 2(b)), the thickness H and the relative density of the TPMS cells are the same, and the structure is called homogeneous TPMS. In the case of gradient TPMS cells, the value of the curve can be set as a function of x , y , or z as the independent variable in the X , Y , and Z axes, respectively, e.g., extending the value of C into a linear function that varies with the value of the Z direction.

$$C = Az + B \quad (3)$$

where A and B are constants, the value of C can be obtained as a linear grading along the Z -axis direction to achieve the gradient design. It can be clearly observed that when the values are linearly gradient along different coordinate axis directions, the pore size and thickness of the primitive cell unit also change with the corresponding direction, realizing a thin-to-thick variation in its thickness

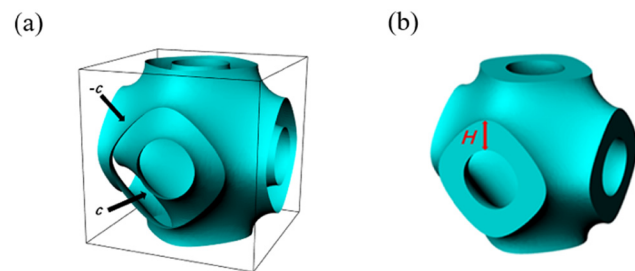


Figure 2: (a) Open dual primitive surface and (b) construction of solid cell of TPMS structure.

while keeping the cell size constant. The relative density of the TPMS structure is defined by Eq. (4). V_{TPMS} denotes the volume of the TPMS structure, and V is the cubic volume.

$$\rho^* = \frac{V_{\text{TPMS}}}{V} \quad (4)$$

The TPMS structure investigated in this study was divided into two types: homogeneous TPMS structure and gradient TPMS structure. The TPMS cell size was 3.75 mm, with 8 cells in each direction (X , Y , Z), resulting in a 30 mm \times 30 mm \times 30 mm structure. To investigate the influence of relative density on the quasi-static mechanical properties of TPMS structures, four relative densities (20, 30, 40, and 50%) were examined for both homogeneous and gradient TPMS structures. All structures were generated by MSLattice software, and the settings of the relative density are shown in Table 1. The length, width, and height dimensions of the specimen are obtained from the Vernier caliper to obtain the cubic volume V . The weight of the specimen is obtained by the electronic scale and the mass-volume conversion formula is used to obtain the volume V_{TPMS} of the structure. Then, the actual relative density is calculated using the formula V_{TPMS}/V . And the wall thicknesses are obtained by optical microscope. The specimens were made of ClearV4 resin polymer with a material density of 1.169 g·cm⁻³ and Young's modulus of 850 MPa. The parameters used in SLA refer to the literature of Bai *et al.* [23].

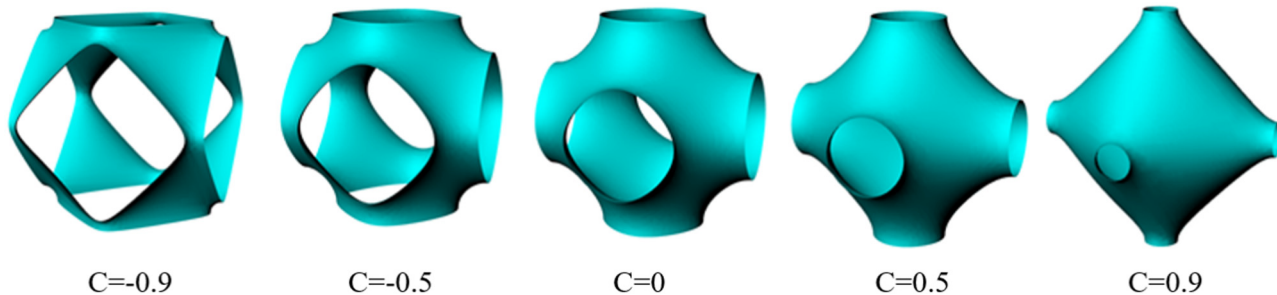


Figure 1: Primitive surface form when C value changes.

Table 1: Parameters of TPMS design model and experimental specimen

	Name of test piece	C value	Design relative density (%)	Actual relative density (%)
Homogeneous TPMS structure	P-U-1	0.340	20.00	26.63
	P-U-2	0.508	30.00	36.34
	P-U-3	0.678	40.00	44.94
	P-U-4	0.851	50.00	54.03
Gradient TPMS structure	P-G-1	$0.243 + 0.005z$	20.00	25.66
	P-G-2	$0.42 + 0.006z$	30.00	37.90
	P-G-3	$0.42 + 0.017z$	40.00	45.85
	P-G-4	$0.42 + 0.018z$	50.00	54.74

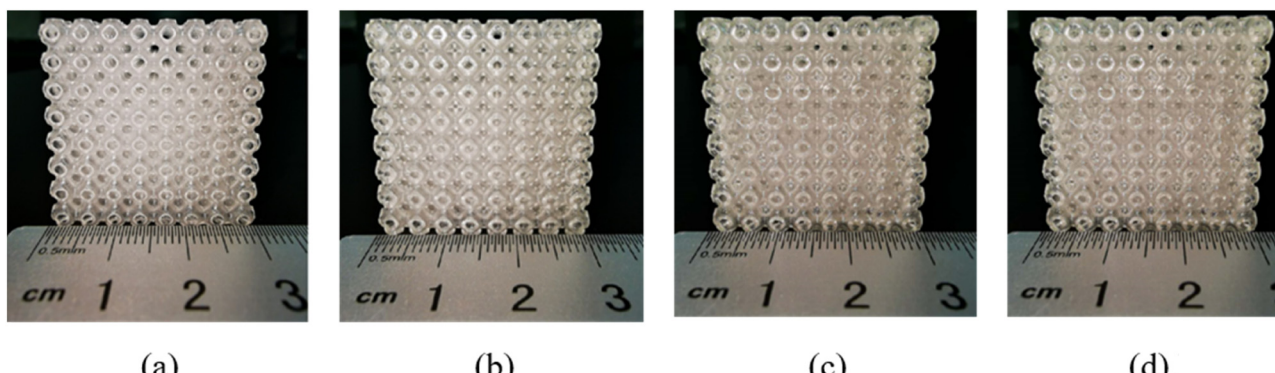
Low Force Stereolithography (LFS) was used to reduce the peeling force applied to the printed part during the printing process, and linear illumination and a flexible tank were employed to cure the resin. Linear illumination involves brief laser irradiation to make the liquid print material solid at high temperatures, enhancing its stiffness and stress. The flexible tank was used to smooth the surface of the specimen and fill laser pits and small cracks on the surface, greatly improving the surface quality and printing accuracy of the printed parts. The size of the cell was carefully designed to ensure that the liquid resin attached inside the cell could be removed cleanly by alcohol, minimizing printing errors and improving printing accuracy. The specimens are depicted in Figures 3 and 4.

The quasi-static compression experiments were performed on the TPMS structures using the Instron 5567 test machine manufactured by Instron Corporation, USA, as shown in Figure 5(a). During the experiment, the TPMS structures were positioned freely between the upper and lower platens with no additional constraints. To ensure even contact between the loaded platen and the specimen, both platens were kept horizontal, and the specimens were centered as much as possible, as shown in Figure 5(b). Compression was controlled by regulating the loading rate, with a loading strain rate of 0.001s^{-1} ; the loading

rate was $0.03\text{ mm}\cdot\text{s}^{-1}$. TPMS specimens produced through SLA AM technology exhibit high accuracy, excellent printing precision, and surface finish. This ensures that the TPMS specimens can maintain a stable deformation mode. Therefore, this study uses only one sample for each structure for mechanical tests. At the same time, FEA is used to verify the results, and the FEA results agree with the experimental results.

The FEA is carried out through Abaqus software in this study. Hexahedral meshes are used for all the structures, and “Dynamic, Explicit” is used for the analysis step. General contact (Explicit) is selected for the interaction, using the “Penalty” with 0.3 and the “Hard” contact for the contact properties. The material, ClearV4, was modeled as an elastoplastic material, and the elastic and plastic material parameters of ClearV4 are listed in Tables 2 and 3, respectively. The SLA fabricated bulk material has Young’s modulus of 850 MPa and yield strength of 8.517 MPa based on in-house tensile testing according to ASTM E8/E8M[39] and may be considered isotropic. A Poisson’s ratio of 0.36 for ClearV4 is adopted in FE simulations.

In this study, three main parameter metrics were utilized to analyze the energy absorption of the two TPMS structures under quasi-static axial compression loading. These metrics include the absorbed energy (AE), SEA, and initial peak crushing force (PCF) [40,41]. The AE is

**Figure 3:** 3D printed homogeneous TPMS structure specimens. (a) P-U-1, (b) P-U-2, (c) P-U-3, and (d) P-U-4.

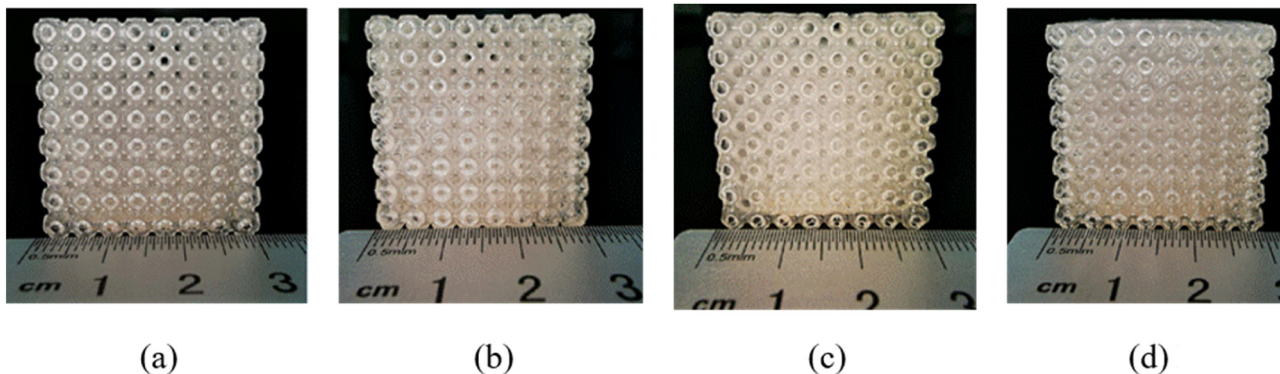


Figure 4: 3D printed gradient TPMS structure specimens. (a) P-G-1, (b) P-G-2, (c) P-G-3, and (d) P-G-4.

calculated by determining the TPMS wall thickness and using a specific expression to calculate the energy absorbed by the structure receiving axial loading.

$$AE = \int_0^l F(z)dz \quad (5)$$

where l denotes the displacement required for the TPMS structure to enter the densification stage by axial compression, z denotes the compression displacement, and $F(z)$ is the change in pressure as a function of compression displacement. SEA is represented as the energy absorption per unit mass of the TPMS structure and is expressed in Eq. (6).

$$SEA = \frac{AE}{m} = \frac{\int_0^l F(z)dz}{m} \quad (6)$$

where m is the actual mass of the TPMS structure, the implications of the mass of the structure need to be

Table 2: Elastic material parameters of ClearV4 resin polymer

Young's modulus	Poisson's ratio
850 MPa	0.36

Table 3: Plastic material parameters of ClearV4 resin polymer

Plastic strain	True stress (MPa)
0	8.517
0.006	18.213
0.023	22.865
0.051	25.491

considered in the study of porous structures, and SEA, which measures the efficiency of energy absorption, is an

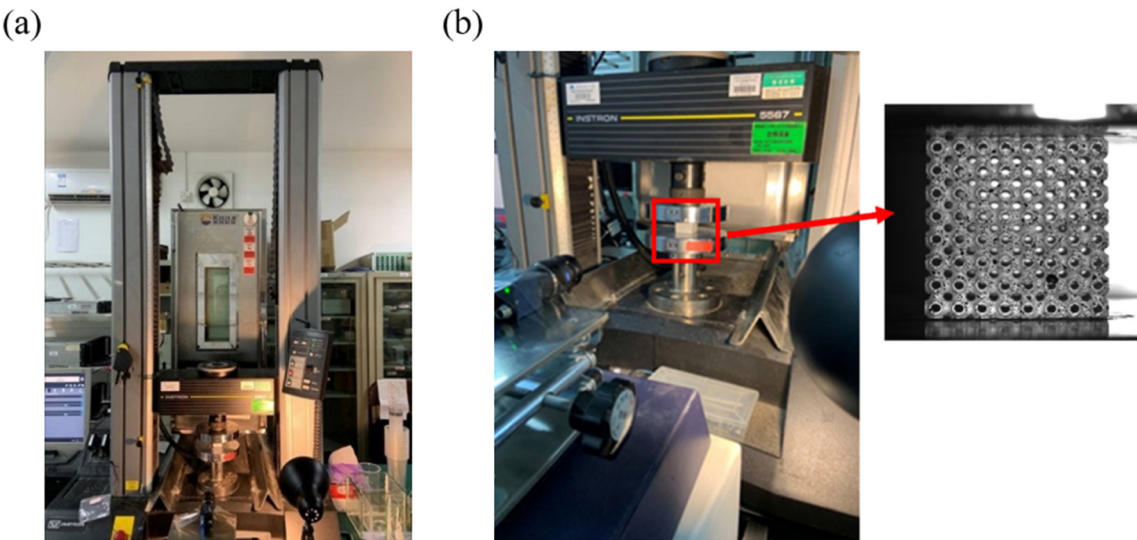


Figure 5: (a) Test machine Instron 5567 and (b) specimens under quasi-static compression test.

important metric. The PCF expressed as the peak value of the first crest in the force–displacement curve of the TPMS structure when loaded by axial compression is a critical metric that is often used to predict the dynamic properties of the structure, implying a relationship with acceleration and thus controlling the intrusion velocity and acceleration. When the PCF is smaller, the TPMS structure is more stable during collision and has better impact resistance [40].

The Gibson-Ashby model of porous structures [42] is used to analyze the mechanical properties of TPMS structures in relation to their relative density. This model allows us to describe the normalized plateau stress ($\sigma_{\text{pl}}/\sigma_y$), normalized compression modulus (E/E_s), and energy absorption W of TPMS structures using a power law dependent on density.

$$\phi_{\text{cellular}} = C\rho^n \quad (7)$$

where ϕ_{cellular} represents the mechanical properties of the structure, ρ is the actual relative density of the structure, C is a geometric parameter, and n is the curve-fitting index. E_s and σ_y are Young's modulus and yield strength of the base material ClearV4, respectively. σ_{pl} is the plateau stress of the structure, which is taken as the arithmetic mean of the stresses of the structure in the interval from 20 to 40% of the compressive strain [43], and W denotes the value of the energy absorption of the TPMS structure under compressive loading.

resolution is 5 nm. A thin layer of metal is deposited on the surface of the sample by vacuum evaporation. The purpose is to improve the resolution of the SEM and to increase the signal strength so that the SEM can show the detailed features of the sample surface more clearly. The SEM morphology analysis of the TPMS structure was conducted at different magnifications, as shown in Figure 6. Figure 6(a) displays the image at 100× magnification, revealing the smooth transition between each cell on the inner wall of the TPMS structure without any angularity. The surface of the specimen exhibits a series of ripple patterns (as seen in Figure 6(b)) resulting from the traces generated through LFS printing technology. In addition, one might observe minute particles on the surface formed from the curing of the printing material solution by linear illumination. Compared to other types of AM techniques [20,44], specimens printed by SLA technology have a much smoother surface and substantially reduce the amount of material powder attached, eliminating the need for special cleaning of SLA-printed specimens.

According to the findings in Table 1, an evaluation was made on the relative density of the TPMS structure design model against the printed specimen. The data show that the actual relative density of TPMS structure specimens is higher than that of the geometric parameters of the finite element design models. The reason for this is that during the process of linear illumination, the print material on the surface of the structure remains and cures with heat. Furthermore, the continuous appearance of pits on the surface caused by the flexible resin groove made it challenging for the printer to fill the structure accurately. Attempting to fill the structure continuously would result in an overflow of material, leaving it on the surface to cure with the specimen. These deviations of the actual TPMS specimens from the geometric parameters of the finite element design models cannot be avoided by AM technology [23,45–47]. However, the deviations of the TPMS specimens are controllable, and

3 Results and discussion

3.1 SEM characterization

The SEM characterization is obtained by (SEC) SNE-4500M Plus. The detection method is secondary electrons, and the

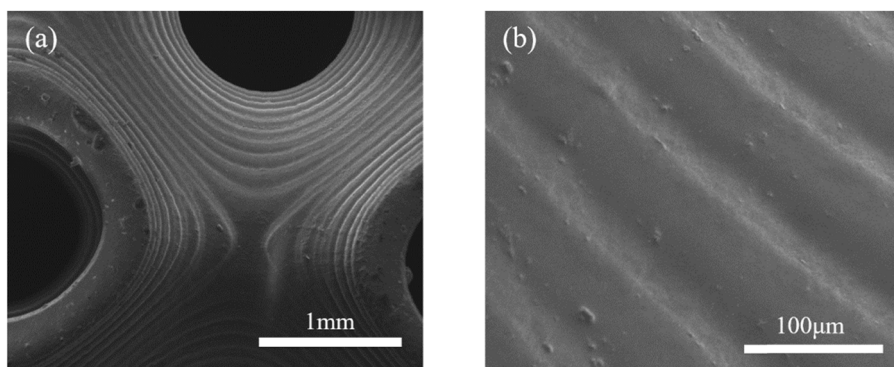


Figure 6: SEM characterization of TPMS structural with (a) 100× and (b) 1,000× magnification.

the specimens do not show any cracks, pores, holes, or other printing defects. This means that the printing results are satisfactory.

3.2 Mechanical properties of the TPMS structure under quasi-static compression

According to the findings in Figure 7, it was observed that the stress-strain curves for both the homogeneous TPMS structure and the gradient TPMS structure exhibited three clearly defined regions. These regions include an elastic phase, which extends from the initial loading until the structure reaches its yield strength (initial peak load), a plastic plateau phase where the structure undergoes deformation in the middle of the loading process, and a densification region where the structure is compressed to a stacked state. Based on the figure presented, it was evident that the numerical simulation results align well with the experimental results. The stress-strain curves obtained from the numerical simulation exhibit a consistent behavior to the experimental stress-strain curves, with three stages: elastic stage, plastic plateau stage, and densification stage. It is interesting to note that the plastic plateaus of the homogeneous TPMS structures are flat and smooth, while gradient TPMS structures exhibit different characteristics, such that the climbing of the plastic plateau segments intensifies with the relative density increases. In particular, the plastic plateau stage curves of the gradient TPMS structure with lower relative densities, such as P-G-1 and P-G-2, follow a flatter trend similar to that of the homogeneous TPMS structures with similar relative densities. However, the plastic plateau stage curves of the gradient TPMS structure with higher relative densities, such as P-G-3 and P-G-4, have a steeper slope than those of the homogeneous structures with similar relative densities. Compared to homogeneous TPMS structures, the gradient TPMS structures with high relative densities have noticeably higher stress and smaller strain when entering the densification stage. This is consistent with the gradient TPMS structure in other research [23].

As shown in Figure 8, the Gibson-Ashby model was utilized to fit the curves of TPMS structural Normalized mechanical properties-relative density based on the numerical results, and the R^2 values of the fitted curves are all greater than 0.9. The mechanical properties of the TPMS structures are observed to increase with the increase in relative density, as shown in Figure 8(a) and (c). The fitting exponent, n , of the gradient TPMS structure, is smaller than the homogeneous TPMS structure. This suggests that the gradient structure exhibits a more gradual decrease in plateau stress and energy absorption profile with decreasing density, providing a greater advantage in the low-density range. When the relative density of the TPMS structure falls below 50%, the gradient TPMS structure boasts a higher plateau stress than the homogeneous TPMS structure. As the relative density increases, the difference between the two structures diminishes. This is because the thickness of both structural cells significantly increases as the relative density of the two types of TPMS structures grows. As a result, the structure with relatively higher density transitions early from the plastic plateau phase to the dense phase

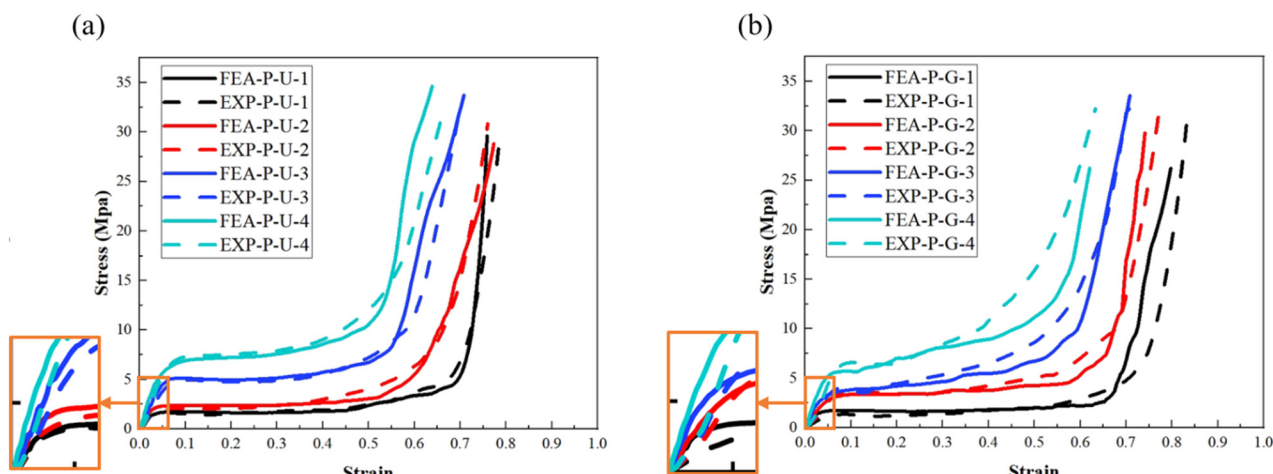


Figure 7: Quasi-static experiments and finite element numerical simulation of stress-strain curves for (a) homogeneous TPMS structures and (b) gradient TPMS structures.

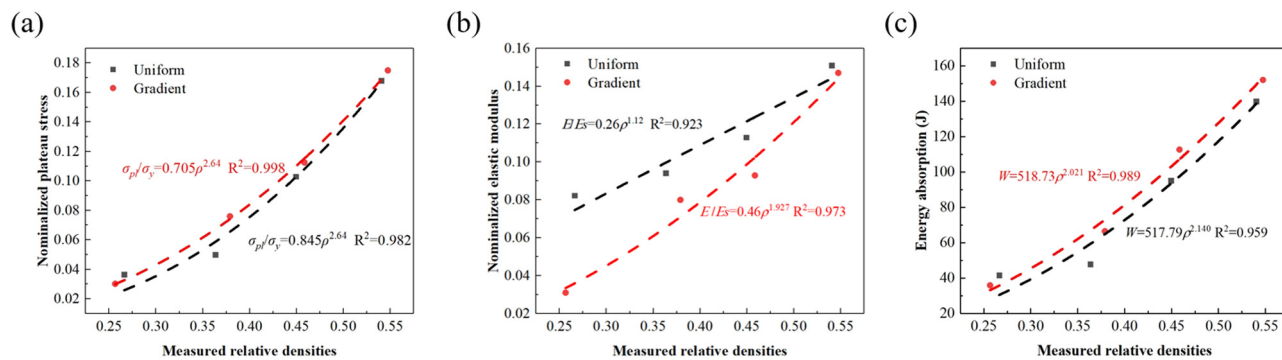


Figure 8: Normalized mechanical properties of TPMS with different relative densities: (a) plateau stress, (b) elastic modulus, and (c) energy absorption.

when subjected to a relatively low strain. Therefore, both gradient and homogeneous TPMS structures demonstrate large plateau stresses. Overall, the trend of the curves indicates that the gradient TPMS structure has a higher plateau stress and better energy absorption capacity than the homogeneous TPMS structure under quasi-static compressive loading. The elastic modulus of the homogeneous structure is higher than that of the gradient structure due to the constant cell thickness of the homogeneous TPMS structure and the larger initial cell thickness of the homogeneous structure compared to the corresponding initial cell thickness of the gradient TPMS structure. Notably, the fitting exponent n is less than 2 for both the TPMS structures, indicating that the TPMS structures are more likely to exhibit a tensile-dominated form of deformation.

Table 4 compares the energy absorption parameters for the homogeneous and gradient TPMS structures obtained from numerical simulations and quasi-static compression experiments. The results indicate that the AE and SEA obtained from numerical simulations for the homogeneous structure are almost identical to the experimental results. A slight deviation is observed for the P-U-4 specimen, where the AE from numerical simulation is 3.6% lower than the

experimental one, and the SEA from numerical simulation is 4.1% lower than the experimental one. Similarly, for the gradient TPMS structure, the AE and SEA obtained from numerical simulations are not significantly different from the experimental results. However, the P-G-4 specimen has a numerically simulated AE that is 4.6% lower than that of the test, and the P-G-3 specimen has a numerically simulated SEA that is 3.5% lower than that of the test. Overall, the EA and SEA errors between the numerical simulation and test of the TPMS structure are within 5%. The finite element simulation of the TPMS structure is highly accurate when compared to the experimental results of the quasi-static compression experiments.

As shown in Table 4, the experimental and numerical simulation data show that the P-G-2, P-G-3, and P-G-4 gradient structures have higher AE and SEA than the homogeneous structures with the same relative density. Additionally, the initial PCF values of P-G-1, P-G-3, and P-G-4 are smaller than their corresponding homogeneous structures, while the PCF of all three gradient TPMS structures are smaller than their corresponding homogeneous structures. For P-G-1, as shown in Table 1, the actual relative density of P-G-1 is smaller than that of P-U-1, and therefore,

Table 4: Comparison of experimental and finite element numerical simulation parameters (AE, SEA, and PCF) for TPMS structures

Model	AE (J)		SEA ($J \cdot g^{-1}$)		PCF (kN)	
	FEA	Exp	FEA	Exp	FEA	Exp
Homogeneous TPMS structure	P-U-1	41.901	41.672	5.211	5.177	1.558
	P-U-2	47.910	47.838	4.362	4.356	2.151
	P-U-3	94.844	95.194	6.985	7.011	4.616
	P-U-4	134.209	139.966	8.160	8.510	6.501
Gradient TPMS structure	P-G-1	37.736	35.941	4.868	4.636	1.571
	P-G-2	60.085	66.543	5.242	5.805	3.072
	P-G-3	108.681	112.73	8.196	8.501	3.511
	P-G-4	145.918	152.119	8.915	9.189	5.146

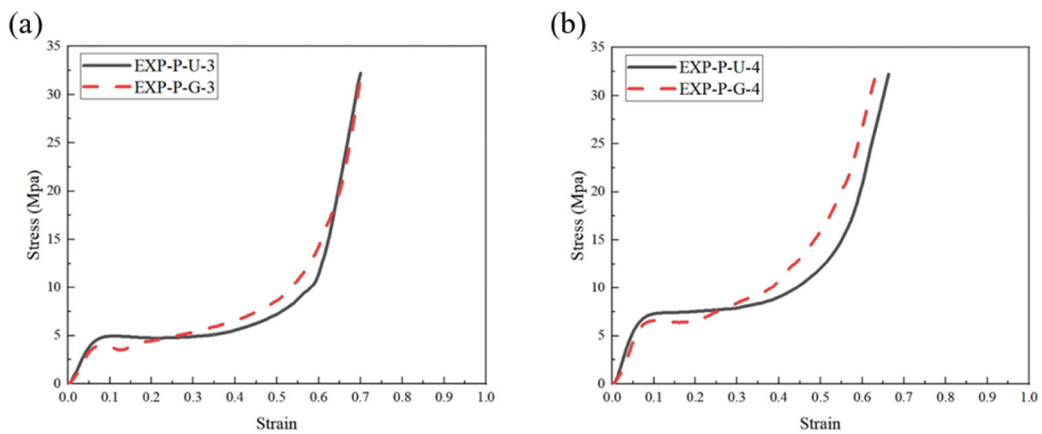


Figure 9: Comparison of stress–strain curves of homogeneous and gradient TPMS structures under quasi-static experiments, (a) P-U-3 and P-G-3, and (b) P-U-4 and P-G-4.

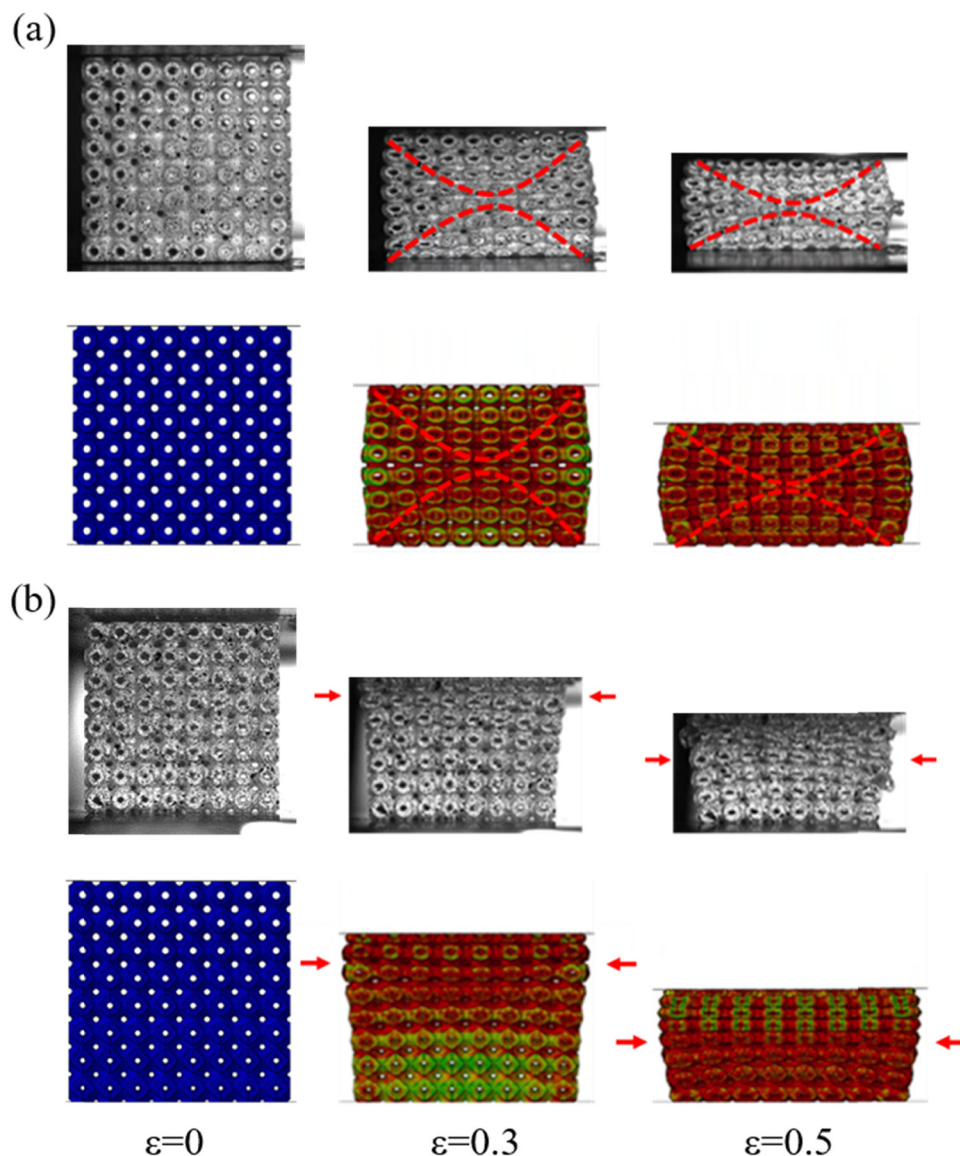


Figure 10: Comparison of experimental and finite element numerical simulation's deformation patterns of (a) P-U-3 and (b) P-G-3 under quasi-static compressions.

the AE and SEA of P-G-1 are smaller than those of P-U-1. The gradient effect of P-G-2 is less obvious because of the lower slope of C , so the plastic plateau curves of P-G-2 do not reflect the stress-strain curves of the gradient structure of the TPMS. The difference between the maximum and minimum thickness of P-G-2 and the thickness of P-U-2 is small, leading to deformation and destruction soon after the elastic phase in the cell layer with the same thickness as P-U-2. This may be the main reason the PCF values of P-G-2 are larger than those of P-U-2. The gradient effect in the P-G-3 and P-G-4 structures is more pronounced than in other gradient structures due to the larger interval between changes in both the shape and thickness of the

specimen. Therefore, to examine the contrast between the homogeneous and gradient structures, P-U-3, P-G-3, P-U-4, and P-G-4 will be further compared with the stress-strain curves, as shown in Figure 9.

In the case of a homogeneous TPMS structure, the thickness of each cell wall is uniform, resulting in consistent yield strength across all layers when compressed. During the plastic plateau phase of axial compression, all cells experience equal pressure, while the cells within each layer undergo intercellular collapse during the densification phase. Figures 10(a) and 11(a) depict the P-U-3 and P-U-4 deformation patterns, illustrating the deformation process of the homogeneous TPMS structure during axial

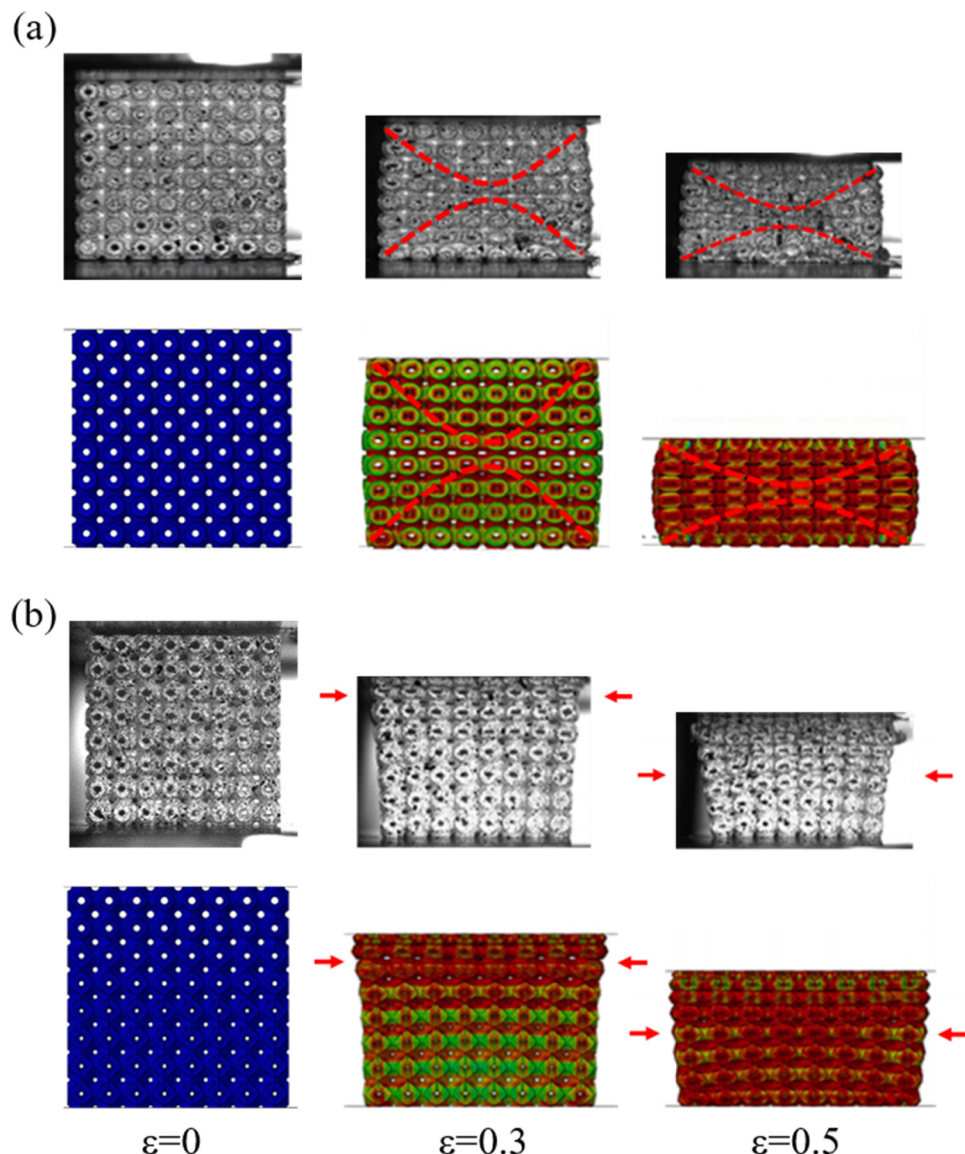


Figure 11: Comparison of experimental and finite element numerical simulation's deformation patterns of (a) P-U-4 and (b) P-G-4 under quasi-static compressions.

compression. During the quasi-static compression process, the structure experiences an initial overall compression, followed by localized deformation in its upper-left, lower-left, upper-right, and lower-right corners. As the cells in the middle region undergo extrusion deformation, the central cell becomes protruded and deformed, resulting in a “damage zone” in the shape of an “X” at 0.3 strain. This zone then gradually expands toward the center along the diagonal during further deformation. These are typical characteristics of a homogeneous TPMS structure. As the compression continues, the overall cell enters the densification stage, ultimately leading to a flattened structure.

The stress-strain curves of the gradient TPMS structure have a pronounced climbing phenomenon in the plateau phase compared to those of the homogeneous TPMS structure, as shown in Figure 7. Furthermore, The comparison of stress strain curves of P-U-3 and P-G-3, and P-U-4 and P-G-4 is shown in Figure 9. Due to the thinner wall thickness of the upper layer compared to the lower layer, the yield strength of the cells in the upper layer is lower than that of the cells in the lower layer. As a result, the stress of the gradient structures demonstrates a steeper climb compared to the homogeneous structure. Unlike the homogeneous TPMS structure, the gradient TPMS structure does not form an “X” damage zone in the middle region. The gradient structure’s deformation behavior

commences with the top layer’s fracture having the smallest thickness, and the specimen collapses in a sequential layer-by-layer pattern. The upper layer cells yield and then collapse, while the lower layer cells provide support. Following the lower layer cells’ yield and collapse, the overall TPMS structure enters the densification stage. Under quasi-static compressive loading, the gradient TPMS structure undergoes cell-layer-by-layer collapse [22], which causes the structural edges to tilt and eventually exhibit a trapezoidal deformation shape with a broad top and a narrow bottom. Because of the cells’ strength inconsistency in each layer, the gradient structure’s smaller wall thickness yields and collapses first in the pre-compression loading stage, resulting in a smaller initial peak force PCF than that of a uniform homogeneous structure with the same relative density.

3.3 Mechanical properties of different gradient types of TPMS structures

Studies have demonstrated that gradient TPMS structures offer better energy absorption properties than homogeneous structures due to their relative density and gradient change rule [23,48]. However, most current gradient TPMS

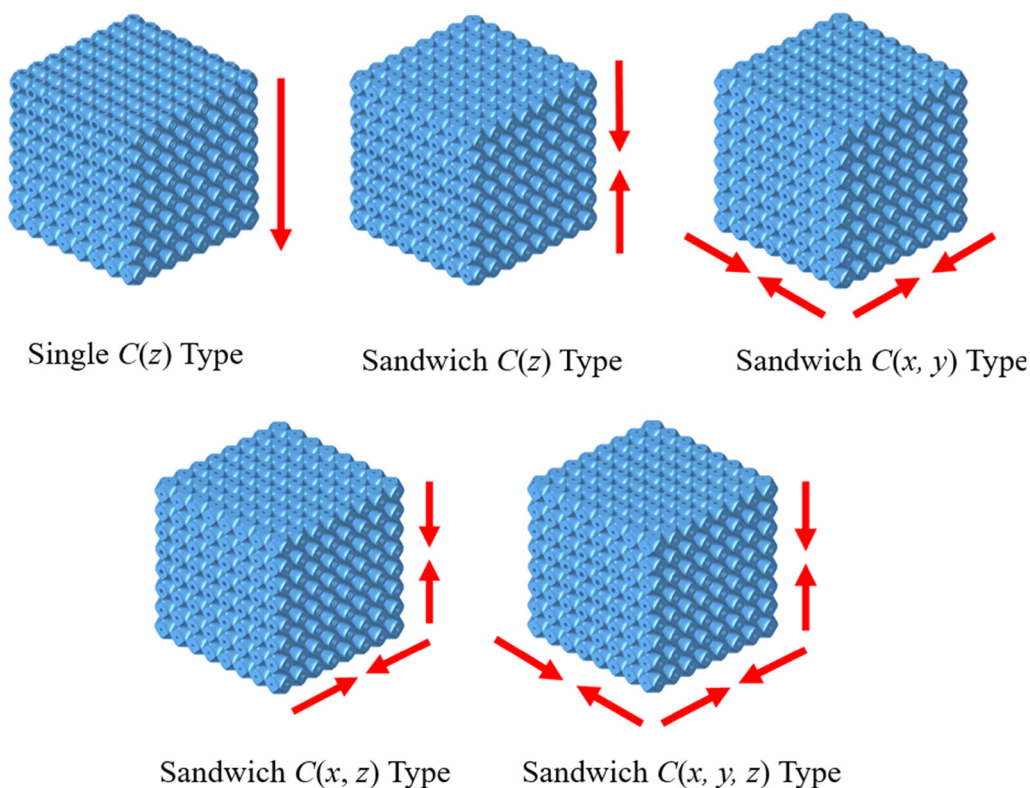


Figure 12: Models of different types of gradient TPMS structures.

Table 5: Parameters of different gradient types of TPMS structures with 40% relative density

	Single $C(z)$ type	Sandwich $C(z)$ type	Sandwich $C(x, z)$ type	Sandwich $C(x, y, z)$ type
Relative density (%)	40			
Maximum thickness (mm)	1.408	1.13	1.299	1.478
Minimum thickness (mm)	0.588	0.746	0.642	0.556
C value	$0.01z + 0.7$	$0.018z + 0.7$	$0.015x + 0.015z + 0.7$	$0.0125x + 0.0125y + 0.0125z + 0.7$

Note: The sandwich structure has symmetry, and the complete sandwich structure is obtained by replicating the structure generated by the C value.

structures only incorporate gradients in one direction. Linear formulae are often used to design gradient TPMS structures of wall thickness to simplify the design process. This study evaluates the mechanical properties of TPMS structures under various gradient types by introducing multi-directional gradient structures and sandwich structures into the conventional TPMS structure design. Quasi-static compression finite element numerical simulations are conducted to investigate the mechanical properties of different gradient types. Using the linear formula in Eq. (3), manipulating the independent variables can determine the C values in the TPMS cell along different directions of change. In designing the gradient TPMS structure, the direction of the Z -axis is selected to be consistent with the compression direction, and a single independent variable, z , is defined along with another in a single vertical direction to obtain different thicknesses. Incorporating gradient variation parameters along both the X and Y -axes into the TPMS formulation's C value allows for the creation of multi-directional gradient TPMS structures, where the C value varies not only in the Z -direction. Furthermore, the sandwich structure can be introduced to obtain the gradient TPMS structure, as shown in Figure 12. In this structure, the slope A and the intercept B in the C value function of each type of structure are kept the same. To ensure easy comparison, each structure type has a relative density of 40%, which keeps the masses constant.

Table 5 shows the parameters of the five gradient TPMS structures with 40% relative density. Depending on the gradient direction, the TPMS structures' maximum and minimum cell thicknesses differ while the relative density, slope, and intercept of the C value function remain constant. The single $C(z)$ Type is the standard gradient structure among the gradient TPMS structures. The gradient direction of the TPMS cell aligns with the compression direction, and the cell population's C value changes linearly with the gradient direction, resulting in varying cell thicknesses from thin to thick. A sandwich structure is incorporated into the design to ensure uniform stress on the compression surface during quasi-static compressive loading. The sandwich $C(z)$ Type sandwich structure features a symmetric TPMS structure that exhibits a gradual change in opposite directions for upper and lower zone cells while maintaining a linear change in C value. The thickness of the TPMS structure's cell is thin in the middle and thick on both sides. In contrast, the sandwich $C(x, z)$ type has a linear change in the C value for cells in both the X and Z directions, allowing the cell thickness of this structure to be thin in the middle and thick on both the Z and X axes. The sandwich $C(x, y)$ type and sandwich $C(x, y, z)$ type structures both have thin middle and thick side cell

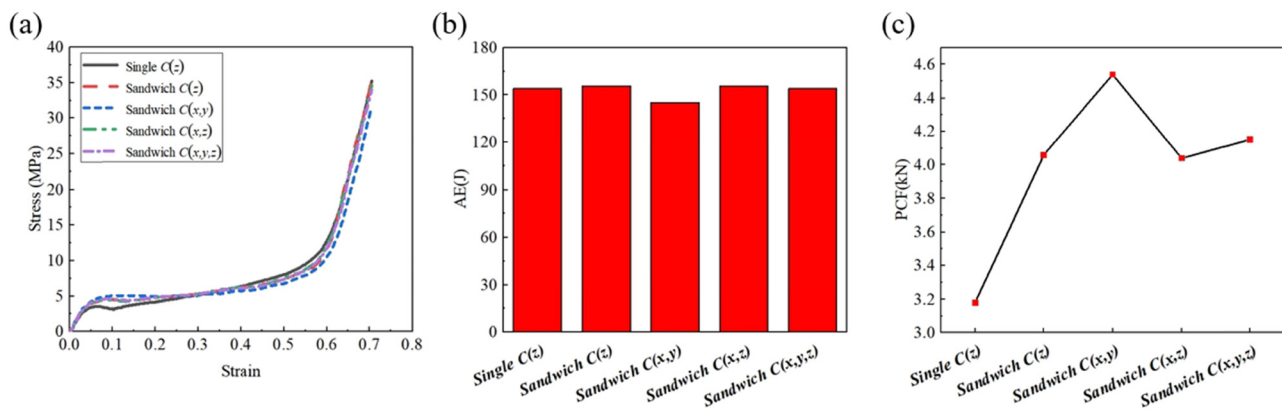


Figure 13: Finite element numerical simulation results of different gradient TPMS structures. (a) Stress–strain curves, (b) energy absorption, and (c) PCF.

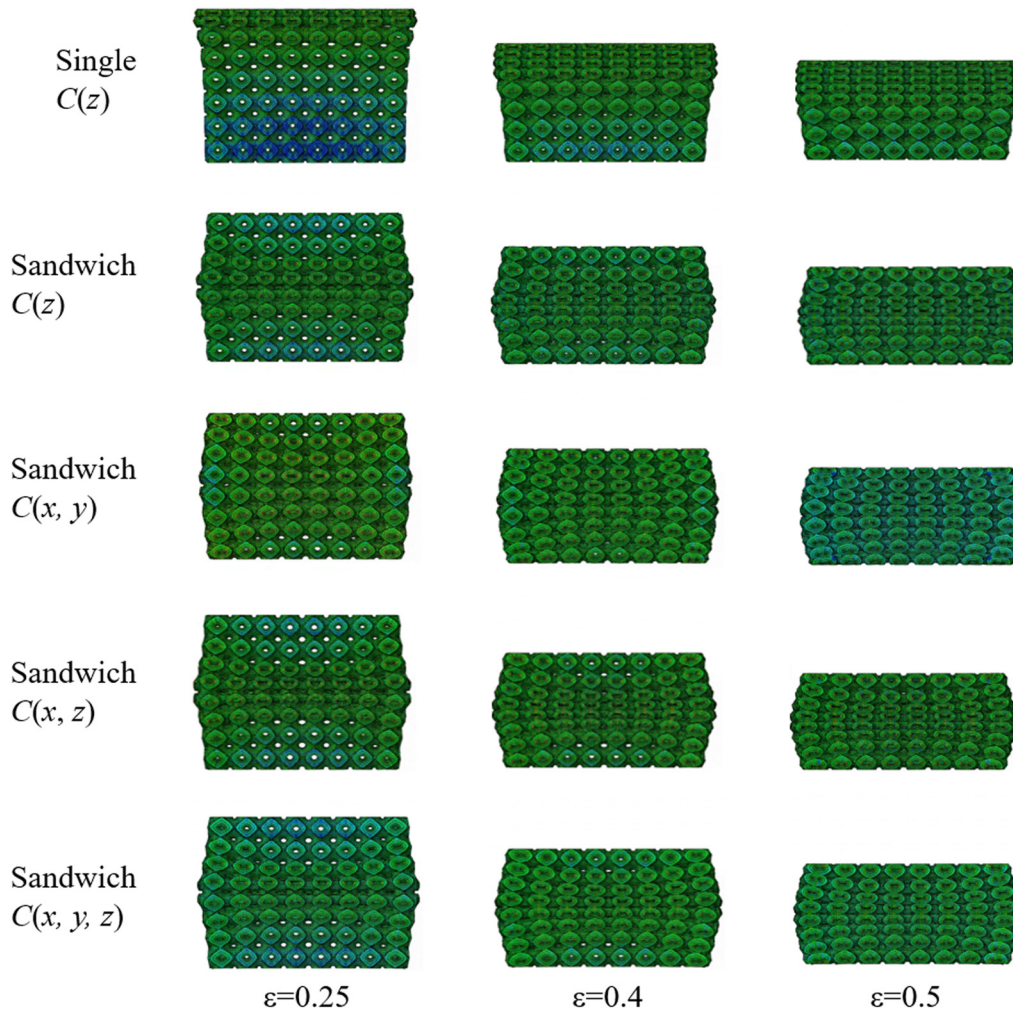


Figure 14: Finite element numerical simulation results of deformation for different gradient TPMS structures.

thickness distributions, but the latter has TPMS cells with linear C value changes in the X , Y , and Z directions, respectively. This structure features thicker cells on the periphery and a thinner center region.

The numerical simulation results of five types of gradient TPMS structures under quasi-static compressive loading are shown in Figure 13. The mechanical properties of TPMS structures with different gradient orientations exhibit significant differences even when the relative density of the TPMS structures and the slope A and intercept B of the C value function are kept constant, as seen from Figure 13(a). The finite element simulation deformation diagrams of gradient TPMS structures given in Figure 14 further confirm this. Among the five types of gradient TPMS structures, the single $C(z)$ type displays a change in cell thickness from thin to thick in the quasi-static compression direction. The smallest thickness cell undergoes breaking during the initial compression process, followed by layer-by-layer destruction of the cell with the largest thickness. Thus, the mechanical properties of this gradient structure exhibit significant differences in different directions, as evident from the stress-strain curves of this gradient structure that maintain an obvious climbing phenomenon.

The sandwich structures have three types of cells: sandwich $C(z)$ type, sandwich $C(x, z)$ type, and sandwich $C(x, y, z)$ type. These cells gradually change in thickness along the compression direction Z . The thinner cells are located in the middle, while the thicker cells are on both sides. During compression, the middle cell group undergoes obvious deformation first, resulting in a climbing phenomenon in the stress-strain curves of the sandwich structures. On the other hand, the quasi-static compression finite element simulation of sandwich $C(x, y)$ type shows a flat and smooth stress-strain curve on the plastic plateau. This may be because the cells of this type of gradient TPMS structures undergo only gradient deformation in the horizontal X and Y directions, while the cells in the compression direction do not have gradient characteristics. Its deformation characteristics are similar to those of homogeneous TPMS structures. In the mid-compression process, an apparent "X" disruption is formed, and the cells of the structure undergo overall deformation that further transitions to the densification stage. Overall, the deformation characteristics of Sandwich $C(x, y)$ type are similar to those of TPMS homogeneous structures.

The energy absorption parameters of five types of gradient TPMS structures are shown in Figure 13(b). The single $C(z)$ type, sandwich $C(z)$ type, sandwich $C(x, z)$ type, and sandwich $C(x, y, z)$ type all have similar total absorbed energies of around 154 J. However, the sandwich $C(x, y)$ type has the smallest total absorption energy, significantly

different from the other four types of gradient TPMS structures. In Figure 13(c), the initial PCF of the single $C(z)$ type is the smallest among the five types of gradient structures, measuring 3.18 kN. The values of the initial PCF of sandwich $C(z)$ type, sandwich $C(x, z)$ type, and sandwich $C(x, y, z)$ type are similar. The sandwich $C(x, y)$ type has the highest initial PCF with 4.54 kN among the gradient structures.

The results show that the gradient structures achieve better energy absorption capacity (higher AE and SEA) and crashworthiness (lower initial peak stresses) when the direction of change of the C value of the TPMS cell aligns with the direction of the structure's compressive loading or when one of the three directions coincides with the force direction. In contrast, the characteristics of the gradient structure cannot be fully embodied when the change direction of the C value of the cell does not align with the structural force direction. The sandwich $C(x, y)$ type has the weakest energy absorption capacity and the highest initial peak force compared to the other four types of gradient TPMS structures. When the gradient direction of the TPMS cell is in the same straight line as the force direction, whether it is a single-direction gradient structure or sandwich structure, the starting point of compression damage is in the weakest region of the structure, and each layer of the cell can fully play the role of cushioning and energy absorption. Therefore, when designing the gradient TPMS structure for cushioning and energy-absorbing materials, the gradient direction of the structure should align with the direction of the material subjected to the load, in addition to increasing its relative density and expanding the interval between the minimum and maximum wall thickness values of the structure, to achieve better cushioning and energy-absorbing efficiency.

4 Conclusion

TPMS specimens produced through SLA AM technology exhibit high accuracy, excellent printing precision, and surface finish, which minimize structural defects and stress drop, and reduces stress fluctuation during compression. This ensures that the TPMS specimens can maintain a stable deformation mode.

As the relative density of the TPMS structure increases, the plateau stress and energy absorption properties are greatly enhanced. Increasing the relative density of the structure is beneficial to the energy absorption properties of the TPMS structure.

The gradient TPMS structure demonstrates superior AE and SEA as well as reduced PCF compared to the

homogeneous TPMS structure. These results indicate that the gradient TPMS structure is a more capable option for energy absorption and impact resistance.

Comparisons of the mechanical properties and deformation mechanisms of gradient TPMS structures of various gradient types show that the gradient TPMS structure with a single-direction gradient structure exhibits superior mechanical properties when the direction of the gradient TPMS cell aligns with the force direction of the structure. This is because the linear variation of the cell C value in a single direction leads to a deformation mode in which the gradient structure is deformed and destroyed layer by layer from the low-density zone, which plays a crucial role in enhancing energy-absorbing properties.

Acknowledgments: The authors would like to acknowledge the support of the National Nature Science Foundation of China (Grant Nos 52178193, 12102097, and 12002094), Natural Science Foundation of Guangdong Province (Grant Nos 2022A1515012086, 2022A1515012037, 2018A030310310, and 2020A1515010915), Guangzhou Municipal Science and Technology Project (Grant Nos 202102021026 and 202102020606), and The Science and Technology Plan Project of Guangzhou (202102010491).

Funding information: The work is supported by the National Nature Science Foundation of China (Grant Nos 52178193, 12102097, and 12002094), Natural Science Foundation of Guangdong Province (Grant Nos 2022A1515012086, 2022A1515012037, 2018A030310310, and 2020A1515010915), Guangzhou Municipal Science and Technology Project (Grant Nos 202102021026 and 202102020606), and The Science and Technology Plan Project of Guangzhou (202102010491).

Author contributions: All authors have accepted responsibility for the entire content of this manuscript and approved its submission.

Conflict of interest: David Hui, who is the co-author of this article, is a current Editorial Board member of *Reviews on Advanced Materials Science*. This fact did not affect the peer-review process. The authors declare no other conflict of interest.

References

- [1] Yin, H. F., W. Z. Zhang, L. C. Zhu, F. B. Meng, J. E. Liu, and G. L. Wen. Review on lattice structures for energy absorption properties. *Composite Structures*, 2023, Vol. 304, id. 116397.
- [2] Wang, H., D. W. Tan, Z. P. Liu, H. F. Yin, and G. L. Wen. On crash-worthiness of novel porous structure based on composite TPMS structures. *Engineering Structures*, 2022, Vol. 252, id. 113640.
- [3] Feng, J. W., J. Z. Fu, C. Shang, Z. W. Lin, and B. Li. Porous scaffold design by solid T-splines and triply periodic minimal surfaces. *Computer Methods in Applied Mechanics and Engineering*, Vol. 336, 2018, pp. 333–352.
- [4] Han, L. and S. A. Che. An overview of materials with triply periodic minimal surfaces and related geometry: FROM biological structures to self-assembled systems. *Advanced Materials*, Vol. 30, 2018, id. 17.
- [5] Guo, X. F., X. Y. Zheng, Y. Yang, X. Y. Yang, and Y. Yi. Mechanical behavior of TPMS-based scaffolds: a comparison between minimal surfaces and their lattice structures. *Sn Applied Sciences*, Vol. 1, 2019, id. 10.
- [6] Peng, C. X., K. Fox, M. Qian, H. Nguyen-Xuan, and P. Tran. 3D printed sandwich beams with bioinspired cores: Mechanical performance and modelling. *Thin-Walled Structures*, 2021, Vol. 161, id. 107471.
- [7] Alkebsi, E. A. A., H. Ameddah, T. Outtas, and A. Almutawakel. Design of graded lattice structures in turbine blades using topology optimization. *International Journal of Computer Integrated Manufacturing*, Vol. 34, No. 4, 2021, pp. 370–384.
- [8] Zhang, Y. F., M. T. Hsieh, and L. Valdevit. Mechanical performance of 3D printed interpenetrating phase composites with spinodal topologies. *Composite Structures*, 2021, Vol. 263, id. 113693.
- [9] Saleh, M., S. Anwar, A. M. Al-Ahmari, and A. Alfaify. Compression Performance and failure analysis of 3d-printed carbon Fiber/PLA composite TPMS lattice structures. *Polymers*, Vol. 14, 2022, id. 21.
- [10] Torquato, S., S. Hyun, and A. Donev. Optimal design of manufacturable three-dimensional composites with multifunctional characteristics. *Journal of Applied Physics*, Vol. 94, No. 9, 2003, pp. 5748–5755.
- [11] Shi, J. P., L. Y. Zhu, L. Li, Z. A. Li, J. Q. Yang, and X. S. Wang. A TPMS-based method for modeling porous scaffolds for bionic bone tissue engineering. *Scientific Reports*, 2018, Vol. 8, id. 7395.
- [12] Li, L., J. P. Shi, K. J. Zhang, L. F. Yang, F. Yu, L. Y. Zhu, et al. Early osteointegration evaluation of porous Ti6Al4V scaffolds designed based on triply periodic minimal surface models. *Journal of Orthopaedic Translation*, Vol. 19, 2019, pp. 94–105.
- [13] Pare, A., B. Charbonnier, P. Tournier, C. Vignes, J. Veziers, J. Lesoeur, et al. Tailored three-dimensionally printed triply periodic calcium phosphate implants: A Preclinical study for craniofacial bone repair. *ACS Biomaterials Science & Engineering*, Vol. 6, No. 1, 2020, pp. 553–563.
- [14] Hsieh, M. T., M. R. Begley, and L. Valdevit. Architected implant designs for long bones: Advantages of minimal surface-based topologies. *Materials & Design*, 2021, Vol. 207.
- [15] Fan, X. J., Q. Tang, Q. X. Feng, S. Ma, J. Song, M. X. Jin, et al. Design, mechanical properties and energy absorption capability of graded-thickness triply periodic minimal surface structures fabricated by selective laser melting. *International Journal of Mechanical Sciences*, 2021, Vol. 204, id. 106586.
- [16] Wang, X. Z., X. H. Xu, and Y. Gu. Dynamic response of Voronoi structures with gradient perpendicular to the impact direction. *Reviews on Advanced Materials Science*, Vol. 61, No. 1, 2022, pp. 513–525.
- [17] Chen, M. S., J. Liu, T. Zhu, editors, Research on design method of gradient porous support based on triply periodic minimal surfaces, *Annual IEEE International Conference on Manipulation, Manufacturing and Measurement on the Nanoscale (3M-NANO)*. Xian, Peoples R China, 2021 Aug.

- [18] Liu, F., Z. F. Mao, P. Zhang, D. Z. Zhang, J. J. Jiang, and Z. B. Ma. Functionally graded porous scaffolds in multiple patterns: New design method, physical and mechanical properties. *Materials & Design*, Vol. 160, 2018, pp. 849–860.
- [19] Al-Saeedi, D. S. J., S. H. Masood, M. Faizan-Ur-Rab, A. Alomarah, and P. Ponnusamy. Mechanical properties and energy absorption capability of functionally graded F2BCC lattice fabricated by SLM. *Materials & Design*, Vol. 144, 2018, pp. 32–44.
- [20] Chen, C. R., J. F. Ma, Y. M. Liu, G. F. Lian, X. X. Chen, and X. Huang. Compressive behavior and property prediction of gradient cellular structures fabricated by selective laser melting. *Materials Today, Communications*, 2023, Vol. 35, id. 105853.
- [21] Qiu, N., J. Z. Zhang, F. Q. Yuan, Z. Y. Jin, Y. M. Zhang, and J. G. Fang. Mechanical performance of triply periodic minimal surface structures with a novel hybrid gradient fabricated by selective laser melting. *Engineering Structures*, 2022, Vol. 263, id. 114377.
- [22] Ma, X. Y., D. Z. Zhang, M. Zhao, J. J. Jiang, F. Q. Luo, and H. L. Zhou. Mechanical and energy absorption properties of functionally graded lattice structures based on minimal curved surfaces. *International Journal of Advanced Manufacturing Technology*, Vol. 118, No. 3–4, 2022, pp. 995–1008.
- [23] Yu, S. X., J. X. Sun, and J. M. Bai. Investigation of functionally graded TPMS structures fabricated by additive manufacturing. *Materials & Design*, 2019, Vol. 182, id. 108021.
- [24] Fu, J., J. H. Ding, S. Qu, L. Zhang, M. Y. Wang, M. Fu, et al. Improved light-weighting potential of SS316L triply periodic minimal surface shell lattices by micro laser powder bed fusion. *Materials & Design*, 2022, Vol. 222, id. 111018.
- [25] Niknam, H. and A. H. Akbarzadeh. Graded lattice structures: Simultaneous enhancement in stiffness and energy absorption. *Materials & Design*, 2020, Vol. 196, id. 109129.
- [26] Hassan, I. M., T. A. Enab, N. Fouada, and I. Elde souky. Design, fabrication, and evaluation of functionally graded triply periodic minimal surface structures fabricated by 3D printing. *Journal of the Brazilian Society of Mechanical Sciences and Engineering*, Vol. 45, 2023, id. 1.
- [27] Tetsuka, H. and S. R. Shin. Materials and technical innovations in 3D printing in biomedical applications. *Journal of Materials Chemistry B*, Vol. 8, No. 15, 2020, pp. 2930–2950.
- [28] Amin, R., S. Knowlton, A. Hart, B. Yenilmez, F. Ghaderinezhad, S. Katebifar, et al. 3D-printed microfluidic devices. *Biofabrication*, Vol. 8, 2016, id. 2.
- [29] Zhou, T. Y., L. Zhang, Q. Yao, Y. L. Ma, C. Hou, B. H. Sun, et al. SLA 3D printing of high quality spine shaped β -TCP bioceramics for the hard tissue repair applications. *Ceramics International*, Vol. 46, No. 6, 2020, pp. 7609–7614.
- [30] Zheng, X. Y., Z. B. Fu, K. Du, C. Y. Wang, and Y. Yi. Minimal surface designs for porous materials: from microstructures to mechanical properties. *Journal of Materials Science*, Vol. 53, No. 14, 2018, pp. 10194–10208.
- [31] Ma, S. H., K. L. Song, J. Lan, and L. Ma. Biological and mechanical property analysis for designed heterogeneous porous scaffolds based on the refined TPMS. *Journal of the Mechanical Behavior of Biomedical Materials*, 2020, Vol. 107, id. 103727.
- [32] Wu, R. H., Y. F. Li, M. D. Shen, X. Y. Yang, L. Zhang, X. R. Ke, et al. Bone tissue regeneration: The role of finely tuned pore architecture of bioactive scaffolds before clinical translation. *Bioactive Materials*, Vol. 6, No. 5, 2021, pp. 1242–1254.
- [33] Zhang, C., Z. L. Jiang, L. Zhao, W. W. Guo, Z. X. Jiang, X. D. Li, et al. Mechanical characteristics and deformation mechanism of functionally graded triply periodic minimal surface structures fabricated using stereolithography. *International Journal of Mechanical Sciences*, 2021, Vol. 208, id. 106679.
- [34] Makogon, A., S. Balabanov, K. Koshevaya, and M. Sychov, editors. Impact of modeling method on geometry and mechanical properties of samples with TPMS structure, *International Conference on Global Research and Education*, Springer, 2021.
- [35] Wang, E. S., F. Yang, X. M. Shen, Z. Z. Li, X. C. Yang, X. P. Zhang, et al. Investigation and Optimization of the Impact of Printing Orientation on Mechanical Properties of Resin Sample in the Low-Force Stereolithography Additive Manufacturing. *Materials*, Vol. 15, 2022, id. 19.
- [36] Yoo, D. J. Computer-aided Porous Scaffold Design for Tissue Engineering Using Triply Periodic Minimal Surfaces. *International Journal of Precision Engineering and Manufacturing*, Vol. 12, No. 1, 2011, pp. 61–71.
- [37] Jia, H. R., H. S. Lei, P. D. Wang, J. X. Meng, C. L. Li, H. Zhou, et al. An experimental and numerical investigation of compressive response of designed Schwarz Primitive triply periodic minimal surface with non-uniform shell thickness. *Extreme Mechanics Letters*, 2020, Vol. 37, id. 100671.
- [38] Alketan, O. and R. Abu Al-Rub. MSLattice: A free software for generating uniform and graded lattices based on triply periodic minimal surfaces. *Material Design & Processing Communications*, 2020, Vol. 3, id. e205.
- [39] ASTM E8/E8M-16a, *Standard Test Methods for Tension Testing of Metallic Materials*, ASTM International, West Conshohocken, PA, 2016.
- [40] Yin, H. F., D. W. Tan, G. L. Wen, W. Y. Tian, and Q. K. Wu. Crashworthiness analysis and optimization design of TPMS-filled structure. *Material Design & Processing Communications*, Vol. 27, No. 5, 2022, pp. 1481–1498.
- [41] Fang, J. G., G. Y. Sun, N. Qiu, N. H. Kim, and Q. Li. On design optimization for structural crashworthiness and its state of the art. *Structural and Multidisciplinary Optimization*, Vol. 55, No. 3, 2017, pp. 1091–1119.
- [42] Gibson, L. J. Cellular solids. *MRS Bulletin*, Vol. 28, No. 4, 2003, pp. 270–271.
- [43] Mechanical Testing of Metals. Ductility testing. *Compression test for porous and cellular metals*. ISO, 2012.
- [44] Qiu, N., J. Z. Zhang, C. Y. Li, Y. J. Shen, and J. G. Fang. Mechanical properties of three-dimensional functionally graded triply periodic minimum surface structures. *International Journal of Mechanical Sciences*, 2023, Vol. 246, id. 108118.
- [45] Vijayaventaraman, S., L. Y. Kuan, and W. F. Lu. 3D-printed ceramic triply periodic minimal surface structures for design of functionally graded bone implants. *Materials & Design*, 2020, Vol. 191, id. 108602.
- [46] Jin, M. X., Q. X. Feng, X. J. Fan, Z. C. Luo, Q. Tang, J. Song, et al. Investigation on the mechanical properties of TPMS porous structures fabricated by laser powder bed fusion. *Journal of Manufacturing Processes*, Vol. 76, 2022, pp. 559–574.
- [47] Zhao, M., D. Z. Zhang, F. Liu, Z. H. Li, Z. B. Ma, and Z. H. Ren. Mechanical and energy absorption characteristics of additively manufactured functionally graded sheet lattice structures with minimal surfaces. *International Journal of Mechanical Sciences*, 2020, Vol. 167, id. 105262.
- [48] Choy, S. Y., C. N. Sun, K. F. Leong, and J. Wei. Compressive properties of functionally graded lattice structures manufactured by selective laser melting. (Vol. 131, pg 112, 2017) *Materials & Design*, Vol. 140, 2018, id. 451.